Structural and mechanical characterisation of nylon fibre aggregates.

L. Gey, R. Guenin, P. Le Gal, and G. Verhille*

Aix Marseille Univ., CNRS, Centrale Méditerranée,

IRPHE, F-13013 Marseille, France

(Dated: February 25, 2025)

arXiv:2502.15736v1 [cond-mat.soft] 6 Feb 2025

Abstract

The study of fibre networks is of great importance due to their appearance in a wide range of natural and industrial processes. These networks are particularly complex because their properties depend not only on the characteristics of individual fibres but also on their collective arrangements within the network. In this study, we investigate the case of nylon fibre aggregates that were generated in a turbulent von Kármán flow. The key properties of these aggregates are characterized, including their three-dimensional structures, analysed through X-ray tomography, and their mechanical responses. The results are compared with those observed for aegagropilae, a natural fibre aggregate commonly found on the Mediterranean sea shore

I. INTRODUCTION

A wide range of materials consists of an ensemble of elongated objects. The biological world offers numerous examples, with filaments appearing at various scales and in diverse organizations, serving a wide range of functions, from macromolecular networks of cytoskeleton at the scale of a cell to centimetre long collagen aggregates in tendons [1]. Structures formed from elongated objects can also be man-made. For instance, nonwovens, composed of long entangled fibres, can be used for thermal or sound insulation [2] and filtration [3]. Similarly, the paper industry relies on cellulose fibres to create strong yet lightweight sheets. These fibrous structures are valued for their remarkable emergent properties, such as a low volume fraction combined with a high mechanical strength [1]. However, understanding how the microscopic features of the individual fibres relate to the macroscopic properties of the random fibre network remains an ongoing challenge [1, 4, 5].

A notable study of fibre packing is the aegagropilae (or sea ball) [6]. These sea balls are dense, nearly spherical balls formed by entangled fibrous remains of Posidonia oceanica, which accumulate and deposit on the seashores of the Mediterranean Sea [7].

In this study, dense spherical aggregates of nylon fibres are formed in a turbulent von Kármán flow. Their structural an mechanical properties are characterized and compared with those of natural aegagropilae. The content of this paper is as followed. In section II, we present the experimental setup leading to the formation of fibres aggregate. In section III,

* L.Gey mail :lucas.gey@univ-amu.fr

X-Ray tomographic images are used to characterise some of the structural properties of the aggregate. Then, in section IV, the effective mechanical properties of the aggregates is probed through mechanical indentation tests.

II. EXPERIMENTAL SETUP

Nylon fibre aggregates are formed in the laboratory using a von Kármán turbulent flow, as illustrated in Figure 1 (a). The experimental setup consists of a cubic tank filled with water, driven by two counter-rotating smooth disks. The side of the tank is $L_{\mathrm{Box}} = 20\,\mathrm{cm}$ and the radius of the disks is $R_{\mathrm{d}} = 8\,\mathrm{cm}$. The flow is mainly driven by two contra-rotating mean flows associated with axial recirculation. The flow is fully turbulent in the centre part of the tank [8]. The main flow characteristics, measured using PIV without fibres, are summarized in Table I.

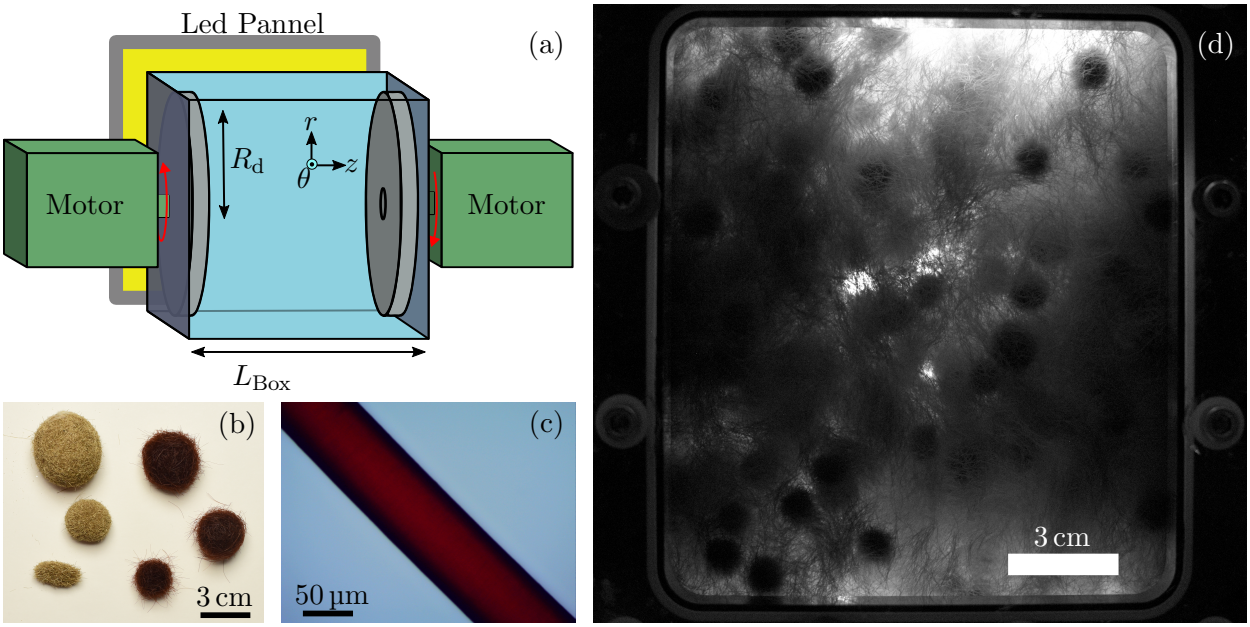


Figure 1: (a) Scheme of the experimental setup. (b) Example of 3 aggregates obtained in the experiment (3 dark red balls on the right on the image), compared with posidonia balls (3 light brown balls of the left side of the image). The black bar measures 3 cm. (c) Image of a fibre taken with a optical microscope with a $\times 40$ magnification. (d) Snapshot of a running experiment.

The main fibres properties can be found in Table I and a microscope view of a fibre is

Table I: Flow and fibers main characteristics

Motor frequency f	2.5 – 21.5 Hz
Root mean squared velocity U_{rms}	4.2×10^{-2} – $3.8 \times 10^{-1}\,\mathrm{m\,s^{-1}}$
Dissipation rate ϵ	1×10^{-4} – $2 \times 10^{-1}\,\mathrm{m^2\,s^{-3}}$
Kolmogorov length $\eta = \left(\frac{\nu^3}{\epsilon}\right)^{1/4}$	4.7×10^{-2} – 3.2×10^{-1} mm
Reynolds number at Taylor scale $Re = \frac{U_{\mathrm{rms}}\lambda}{\nu}$	6.8×10^2 – 1.2×10^3
Integral scale L_{i}	2 cm
Fibre length L	(1.00 ± 0.02) cm
Fibre diameter d	(75 ± 2) µm
Fibre density ρ_p	$(1140 \pm 10)\,\mathrm{kg\,m^{-3}}$
Fibre Young Modulus E_{f}	2.9×10^9 Pa

shown in Figure 1 (c). These flexible fibres have a well-defined diameter of 75 µm and a length 1 cm (aspect ratio of 133.3). They possess a smooth surface texture. A couple of millions of these fibres are introduced in the tank prior to the start of the motors, selecting a volume fraction of $\phi_{\mathrm{Bulk}} \sim 1 \times 10^{-2}$. Then, the motors are operated at a high frequency (25 Hz for 10 min) to ensure that no pre-existing aggregates remain in the system. After this initial phase, the rotation speed is reduced to the target frequency used in the study. Specifically, the results presented in this article correspond to two tested disk rotation frequencies: 7 Hz and 9 Hz.

The experiments are conducted over several hours, with durations ranging from 1 h to 48 h, during which aggregates start to form. This process is illustrated in Figure 1 (d). At the end of the experiment, the aggregates are manually collected and subsequently dried for further analysis. The number of fibres contained in an aggregate is ranging form 10^3 to 10^4. The concentration of the suspension, the fibre dimensions, and the turbulence intensity result in a wide range of aggregate properties. Their numbers range from no aggregates to about 500 aggregates and their sizes from 0.7 cm to 2 cm in radius. The relation between the input parameters and the formation or not of the aggregates and their output properties will be addressed in another article. Here we will only focus on the structural and mechanical properties of the formed aggregates.

An example of the aggregate obtained are presented on Figure 1 (b) in dark red. For comparison, posidonia sea balls are also presented in light brown in Figure 1 (b). Our aggregates are considered spherical, as the mean aspect ratio is of the order of 0.93 ± 0.01. The aggregates are dense and cohesive. They easily maintain their shape under small perturbations such as finger pressure. While the posidonia sea balls are also dense, cohesive and can be spherical, they often exhibit a preferred axis, leading to an aspect ratio of approximately 0.5 [6]. This difference might come from their formation near the sea floor in nature whereas in the lab experiment, the fibres are homogeneously dispersed in the flow.

To better understand how aggregate maintain their coherence, we characterise the structure of the fibre network using X-Ray tomography.

III. X-RAY TOMOGRAPHY

To characterize the fibre network of an aggregate, X-ray tomography is used with an RX Solutions EasyTom XL 150 "Mechanic Ultra" microtomograph. This system is equipped with a sealed micro-focus RX tube operating at 150 kV and a 1920×1536 pixel resolution. The final resolution achieved ranges from 9.8 µm to 18.5 µm, depending on the size of the aggregate.

Following an initial reconstruction using the RX software and binarization, cross-sectional slices of the aggregate can be obtained, as shown in Figures 2 (a) and (b). In these images, the fibres are well-resolved, with approximately six voxels across their diameter. However, the exact contact points between fibres are ambiguous, complicating their separation. To address this difficulty, we implemented a custom algorithm to isolate individual fibres. The process is as follows: i) *Skeletonization:* The 3D volume of the aggregate is skeletonized to identify fibres extremities. ii) *Distance Transform:* A distance transform is applied to the inverted binarized volume, enhancing the central regions of the fibres. iii) *Cylindrical Fitting:* Starting from each extremity, small cylinders are iteratively fitted along the distance-transformed volume. The fitting process is constrained to ensure continuity and forward progression, stopping when the fitted cylinder deviates from the fibre. The cylinder length is set to $L/30$, which is sufficiently long to follow the fibre direction while separating contact points, yet short enough to maintain local accuracy. The cylinders have an overlapping of $L/60$. Indeed, for random hard rods packing, the mean number of contacts per

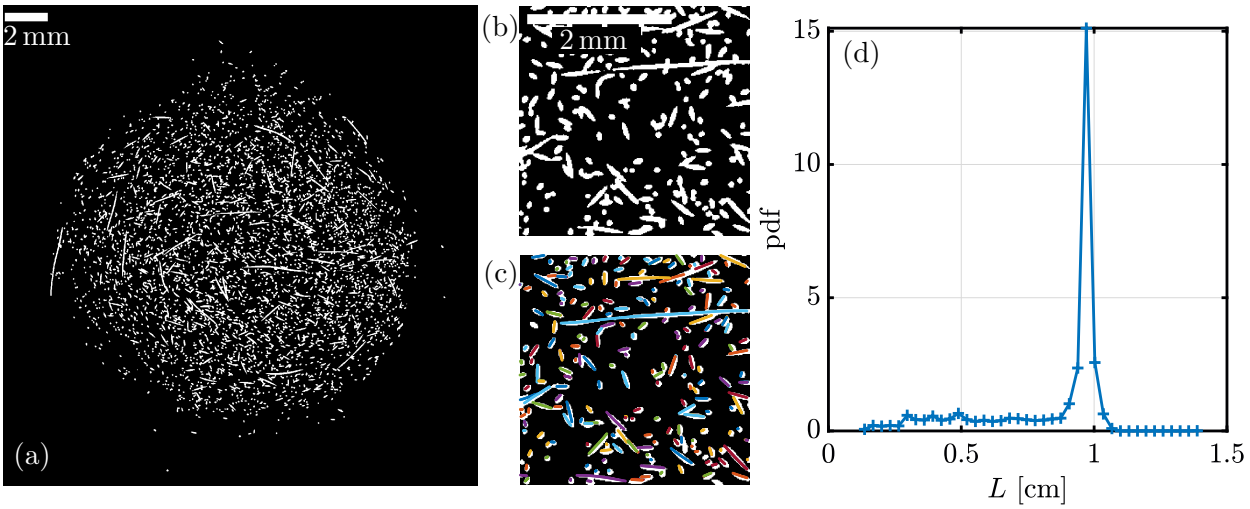


Figure 2: (a) Binarized data of the tomographic reconstruction. (b) corresponds to a zoom of the central region of the image. (c) is the same image on which we added the fit of the fibres separated by colours. (d) Measure of the length of the fibres after reconstruction.

fibre $\langle C \rangle$ is given by $\langle C \rangle \sim \phi L/d$ for $L/d \gg 1$ [4, 9]. This estimation is made using an excluded volume analysis. Extrapolating this formula to our case, with $\phi \sim 0.17$ leads to $\langle C \rangle = 22.6$. iv) *Merging:* Fibres detected from opposite extremities are merged to avoid double-counting. In the end, the fibres are determined by 120 3D coordinates along their length.

The result of this procedure is shown in Figure 2 (c). The algorithm successfully separates fibres, even in cases of contact. However, some fibres are not detected (around 4 %), and occasional duplications occur due to imperfect merging.

Despite these limitations, the histogram of fibre lengths shown in Figure 2 (d) accurately captures the fibre length of around 1 cm, even though the algorithm does not impose a fixed length during the fitting process. The slight gap difference between the expected fibre length, 1 cm, and the measurement, might be explained by the fact that the error on the determination of the extremities is of the order of $L/16 = 0.65$ cm.

Using these tomographic images, we will first characterize the density distribution within the aggregates, followed by an analysis of the coordination number of the fibres and their orientation, and finally, an evaluation of the fibres curvature.

A. Density

The reconstruction data provides access to the volume fraction of the aggregates, as shown in Figure 3 (a). The aggregate are considered to be invariant by rotation which is corroborated by the gray lines in the figure corresponding to the radial evolution of the volume fraction for different conical sectors. This figure shows that the aggregate maintains an approximately constant density up to $r/L \simeq 0.6$, beyond which the density begins to decrease. The drop is gradual rather than abrupt because the aggregates are fuzzy, leading to a reduction in volume fraction at the edges.

The mean volume fraction ϕ_0 of the aggregate is computed using the average volume fraction up to a given radial distance r, represented as $\langle\phi\rangle_r = \frac{1}{r}\int_0^r \phi \, \mathrm{d}r$, as shown in the inset of Figure 3 (a), $r = 0$ corresponding to the centre of mass of the aggregate. The value of ϕ_0 is taken as the maximum of this curve for $r/L > 0.2$, excluding the initial region where measurement error is too high due to the small control volume. A fitting function is used on the tail of $\langle\phi\rangle_r$ in the form $\langle\phi\rangle_r = \frac{a}{r^3} + b$. This function is the expected one for a sphere with a constant density. The intersection between the fit to the tail of $\langle\phi\rangle_r$ and ϕ_0 is used to determine the mean radius R of the aggregate.

Figure 3 (b) shows that the shape of the radial volume fraction profile, $\phi(r)$, is independent of the formation time or motor frequency in the range we tested. This behaviour contrasts with observations for Posidonia sea balls, where the volume fraction increases quadratically with the radial position [6]. A possible explanation for this observation could be that Posidonia sea balls are older aggregates, which results in the adhesion of an increasing number of fibres over time. Additionally, as the aggregate ages, it undergoes more collisions with the surrounding walls or sea bed, leading to a densification of the structure.

In the inset of Figure 3 (b), the analysed X-ray images show that both the mean radius and mean volume fraction increase with Tf, the number of disk rotations. However, due to limited data and significant natural variability, it is not possible to infer a robust scaling law.

The mean volume fraction of the aggregates is approximately $\phi_0 = 0.17$. For comparison, in randomly packed hard rods, the expected volume fraction is $\phi_{\mathrm{rand}}(\frac{L}{d} = 133) \simeq 0.04$. for an aspect ratio of 133 [4]. This indicates that the aggregation process leads to significant compaction compared to random rods packing. The flexibility of the fibres and their inherent

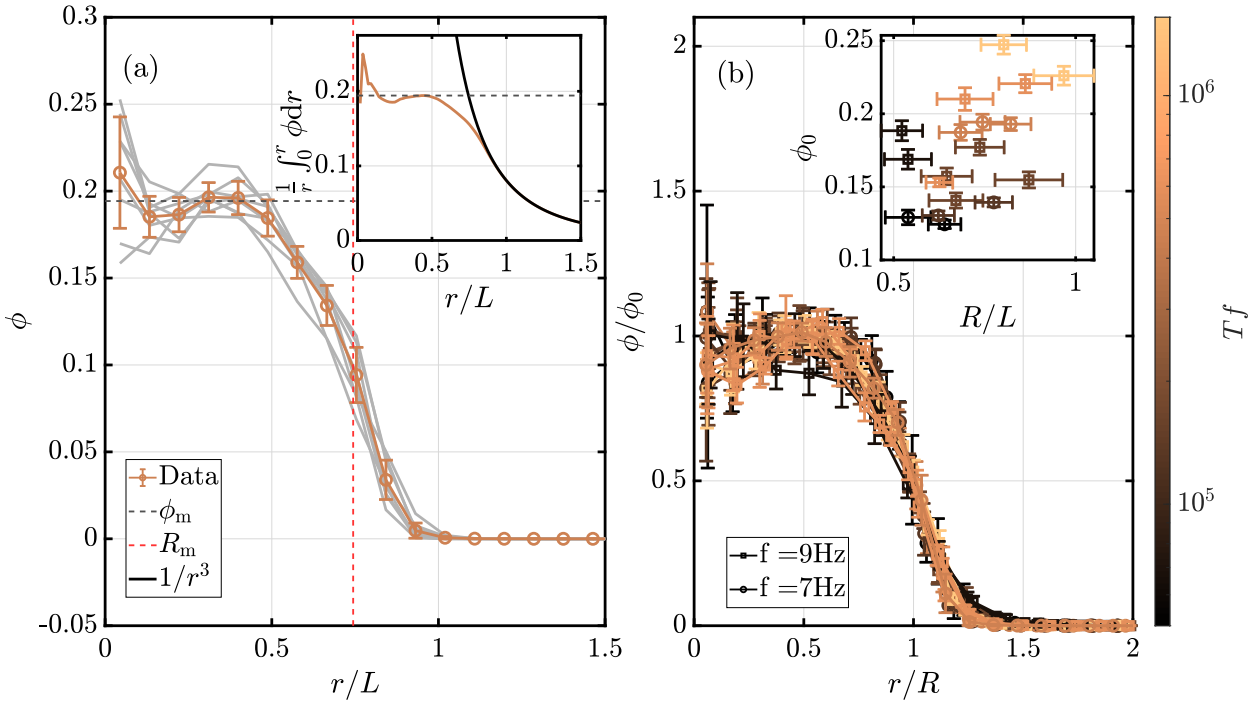


Figure 3: (a) Radial evolution of the volume fraction of fibres within an aggregate. The grey curves correspond to the radial evolution of the volume fraction restricted to conical sector characterized by a angle $\pi/4$. In the inset, the mean volume fraction $\langle\phi\rangle_r$ is plotted as a function of the radius r. The horizontal dashed line represents ϕ_0, defined as the maximum of $\langle\phi\rangle_r$ for $r/L > 0.2$. The black curve is a fit to the latter part of the data in the form $\langle\phi\rangle_r = \frac{a}{r^3} + b$. This fit is used to determine the mean radius R of the aggregate, with $a = \phi_0 R^3$. The values of ϕ_0 and R are indicated on the main graph with black and red dashed lines, respectively. (b) Radial evolution of the volume fraction, normalized by the aggregate size and mean volume fraction, for different aggregates. The inset shows the relationship between the mean volume fraction ϕ_0 and the aggregate radius R, as defined in (a). The colour bar for both figures corresponds to Tf with f the rotation frequency of the motors and T the duration of the experiment. Tf corresponds to the number of rotations of the disks.

curvature are certainly at the origin of this strong compaction.

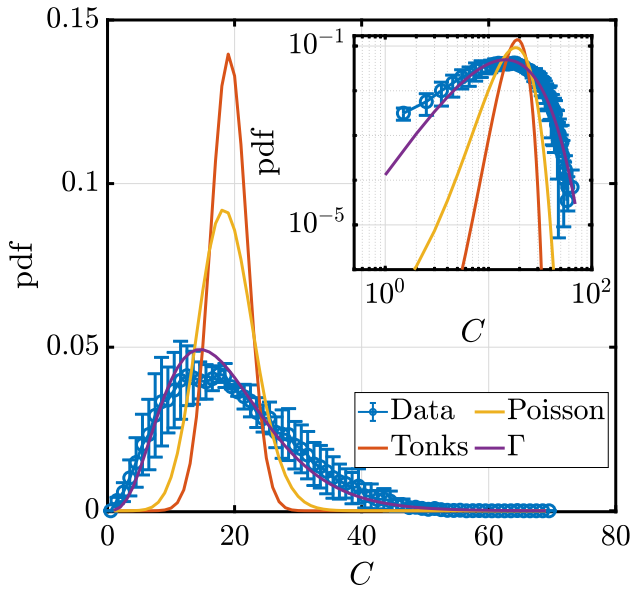


Figure 4: Distribution of the coordination number. Contact are taken into account if the distance between the fibres are less than $1.09d$ and the fibres are interpolated on 120 points. The error bar corresponds to the same data but with a threshold of $1.05d$ and $1.12d$. The yellow curve correspond to the Poisson distribution of parameter $\lambda = \langle C \rangle$. The red curve correspond to the 2 sided Tonks distribution [5] with parameter $d/L = 133$ and imposing that the mean of the distribution correspond to $\langle C \rangle$. The purple curve correspond to a Γ distribution with parameter $\alpha = 4.4$ and $\lambda = 0.23$ calculated from the mean and standard deviation of the data.

B. Coordination Number

The coordination number corresponds to the number of contacts per fibre. This quantity is crucial as it influences the strength of the network.

For hard rods, the mechanical stability of the packing ensures that $4 < \langle C \rangle < 10$ [10]. However, in our case, the fibres are flexible, and the packing is non-random, as discussed in Section III C. This flexibility and organisation introduces additional degrees of freedom, allowing the mean number of contacts per fibre to exceed the upper limit of 10.

In the case of random hard rod packings, the mean coordination number $\langle C \rangle$ is given by [4, 9]:

$$\langle C \rangle \sim \phi \frac{L}{d} \quad \text{for} \quad \frac{L}{d} \gg 1 \tag{1}$$

This estimation is derived from an excluded volume analysis. Applying this formula to our

system predicts $\langle C \rangle = 22.6$. Figure 4 shows the distribution of the coordination numbers. The mean coordination number in our case is $\langle C \rangle = 18.8 \pm 3.8$. The estimation of the coordination number for random packing of rigid fibres, Equation 1, seems still to hold in our case even if fibres are flexible and non randomly packed.

For hard rods, contacts are typically considered point-like and modeled as successive Bernoulli trials, resulting in a Poissonian distribution for the coordination number. This theoretical distribution is shown in Figure 4, but it does not match our experimental data.

When accounting for the finite size of the contacts due to the relative orientation of the fibres, the Tonks' law for a one-dimensional dispersed gas along a line must be considered [5]:

$$P_1(C = N) = \frac{\mu L \left[\mu d_e \left(\frac{L}{d_e} - N + 1\right)\right]^N}{\langle C \rangle_1 N!} \exp\left(-\mu d e \left(\frac{L}{d_e} - N + 1\right)\right) \tag{2}$$

Here, $\mu = \langle C \rangle_1 / (L - \langle C \rangle_1 d_e)$, d_e is the apparent size of the contacts, and $\langle C \rangle_1$ is the mean number of contacts on one side of a fibre.

To account for contacts occurring on all sides of the fibres, Ekman [5] used: $P_n(C = N) = P_1 * P_n(C = N)$. This law is also shown in Figure 4. As expected, incorporating the finite size of the contacts narrows the distribution compared to the Poissonian model. However, it still does not fit our experimental data.

It appears that our data correspond to a Γ distribution:

$$P_\Gamma(C = N) = \frac{\lambda^\alpha}{\Gamma(\alpha)} N^{\alpha-1} \exp(-\lambda N) \tag{3}$$

The Γ distribution, characterized by parameters α and λ, can be interpreted as the sum of α exponential distributions with parameter λ. In our case, this corresponds approximately to four exponential distributions with $\lambda = 0.17$.

C. Orientation

To characterize the angular organization of the aggregate, we define θ as the angle between the radial direction of a point on a fibre and the tangent to the fibre at that point. This is illustrated in Figure 5 (a). The angle $\theta(r)$ is calculated from the coordinates of the parametrised fibres, $X(s)$, using the centre of the aggregate as the origin :

$$\theta = \frac{\vec{\mathbf{X}}(s + \delta s) - \vec{\mathbf{X}}(s - \delta s)}{\left\| \vec{\mathbf{X}}(s + \delta s) - \vec{\mathbf{X}}(s - \delta s) \right\|} \cdot \frac{\vec{\mathbf{X}}(s)}{\left\| \vec{\mathbf{X}}(s) \right\|} \tag{4}$$

and δs is fixed $\delta s = 1\,\text{mm}$.

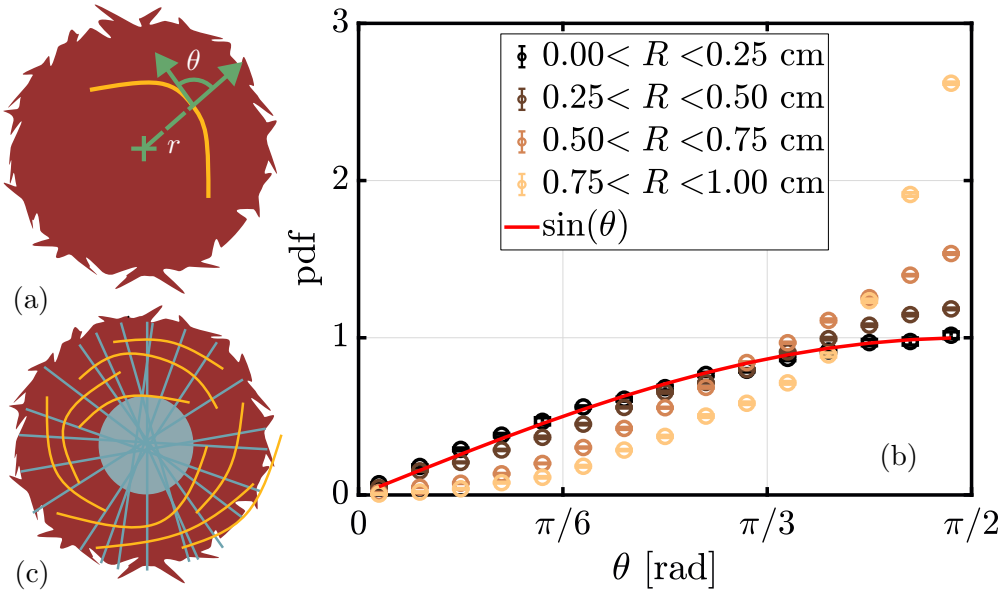


Figure 5: (a) Definition of the angle θ used to characterize the angular distribution of fibres. (b) Distribution of the angle θ for different shells of the aggregate. The error bars correspond to the standard deviation obtained by taking 10 times a random sampling of 80% of the data. In red, the distribution $\sin(\theta)$ corresponding to randomly oriented fibres. (c) Schematic representation of the organisation of the fibres in the aggregate: The blue lines correspond to fibres passing in the core of the aggregate and randomly orientated. The orange lines correspond to fibres wrapped around the aggregate.

Figure 5 (b) shows that the fibre orientations depend on their position within the aggregate. In the core of the aggregate, the fibres are randomly distributed, following a $\sin(\theta)$ distribution (as expected for random orientations due to the solid angle in spherical coordinates). However, in the outer shells, the distribution of θ deviates from the random case, showing a higher proportion of orthoradial fibres.

This observation suggests that fibres are randomly distributed in the core, but new fibres added during the aggregation process, wrap around the aggregate. A similar phenomenon has been observed in posidonia sea balls, where the outer shell also exhibits an excess of orthoradial fibres [6]. However, this trend is much more pronounced in our laboratory aggregates. One possible explanation for this difference is the angle detection. Indeed, for the posidonia sea balls the angle is find by fitting a cylinder on the 3D tomographic images. However there is no history of the fibre for this fit and the angle determination around the

contact points is less precise. Thanks to our fibre separation, this randomisation of the angle θ at the contact point is less pronounced. We have tested to use similar technics on the raw tomographic data with our aggregate, leading to similar results.

D. Curvature

Nylon fibre aggregates are typically expected to be held together by elastic interlocking [11]. As a direct consequence, this interlocking should be visible in the curvature of the fibres. First we estimate the potential curvature of the fibres due to their formation. In our case, the aggregates formed in turbulence. The curvature induced by a fibre in a turbulent flow can be estimated as $\kappa l_\mathrm{e} \simeq a(L/l_\mathrm{e})^3$ [12], where a is a numerical constant, and $l_\mathrm{e} = (EI)^{1/4}/(\eta\rho\epsilon)^{1/8}$ is the elastic length of the fibre in turbulence (η and ρ are the dynamic viscosity and the density of the fluid, respectively). Fitting their data gives $a \simeq 5 \times 10^{-2}$.

Using this model, the expected curvature in our case is on the order of $\kappa \simeq 1\,\mathrm{m}^{-1}$. Figure 6 presents the distribution of the curvature of free fibres compared with that of fibres within aggregates. Contrary to this expectations, the curvature distribution for fibres in aggregates is similar to the one of free fibres. Especially, no significant increase in curvature around $\kappa \simeq 1\,\mathrm{m}^{-1}$ is observed.

For free fibres, the curvature distribution peaks around $\kappa = 1 \times 10^2\,\mathrm{m}$, likely due to the inherent curvature introduced during their production process. This observation indicates that, in our case, the geometry of the fibres can leads to steric effects.

This steric hindrance appears to play a more significant role in the aggregation process than the (unobserved) elastic interlocking mechanism.

In the following section, the structural properties of the aggregates will be linked to their mechanical properties.

IV. MECHANICAL PROPERTIES

In this Section we want to characterize the effective Young modulus of the aggregates by mechanical indentation tests.

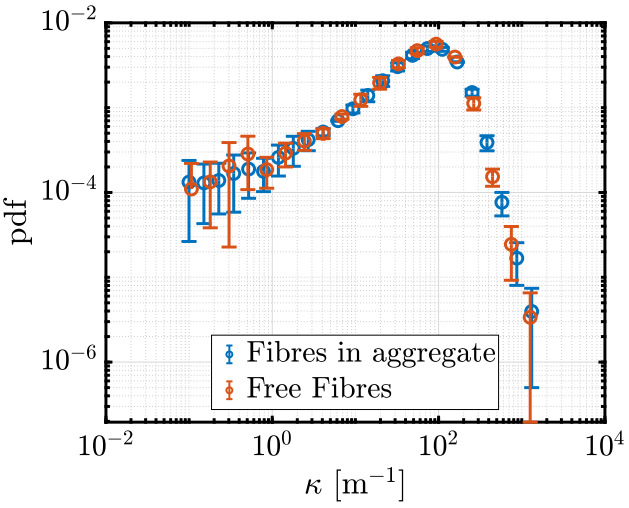


Figure 6: Curvature of the fibres in an aggregate compared with free fibres. The curvature is measured using points separated from a distance $\delta x = L/40$

A. Experimental Setup

The experimental setup illustrated in Figure 7 allow the characterization of the mechanical response of the aggregate to external forces. A ZwickRoell testing machine is used to indent a metal sphere with a radius of $R_{\text{ind}} = 1.5\,\text{mm}$ into the aggregate at a constant velocity of $v_{\text{ind}} = 5\,\text{mm/min}$.

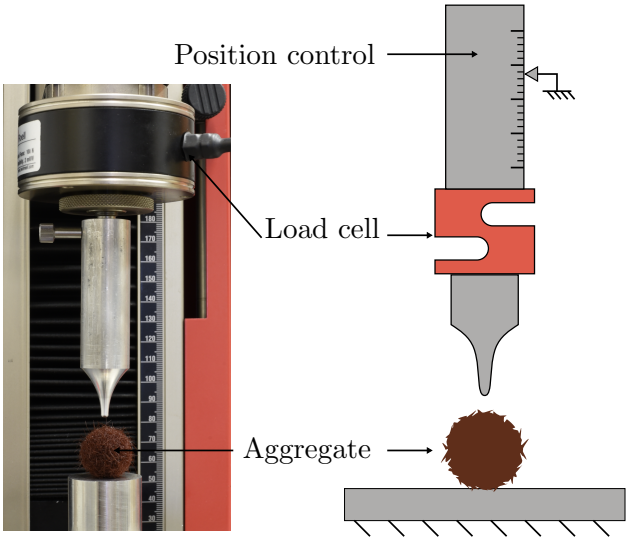


Figure 7: Image and scheme of the experimental setup for the measure of the elasticity of the aggregate. The loading cell is a XForce P with a maximal measuring force of 100 N

A load cell measures the force applied to the aggregate as a function of the indentation

displacement. The indenter size is small relative to the aggregate radius ($R \sim 7\,\mathrm{mm}$) to ensure local measurements, yet large compared to the mean spacing between fibres ($l \sim \frac{L}{\langle C \rangle} \sim 0.5\,\mathrm{mm}$).

An example of 4 loading cycles is presented in the inset of Figure 8 (a). The cycles are naturally shifted relative to one another. This is due to the irregular shape of the aggregate and the presence of protruding fibres, which result in force signals before the indenter fully penetrates the aggregate. For the studied aggregates, the maximum indentation force is set to $F_{\max} = 0.5\,\mathrm{N}$ to avoid drastic reorganization of the fibres between cycles. Nevertheless, a hysteresis loop is observed, indicating energy dissipation during the process. Despite this, each curve exhibits a consistent trend, suggesting that the initial indentation phase remains comparable across cycles.

To characterize the equivalent Young modulus of the aggregates, we focus on the first part of each curve as an example is shown on Figure 8. For small displacement, the response of the aggregate under loading is expected to follow the laws of linear elasticity, hence, for this planar-spheric configuration to follow the Hertz law [13]: $F = \frac{4}{3} E R_{\mathrm{ind}}^{1/2} \delta^{3/2}$. Indeed, for a displacement of $\delta \ll R_{\mathrm{ind}}$ the strain is of the order of $\epsilon \sim \sqrt{\delta / 2R_{\mathrm{ind}}} \simeq 0.4$ for $\delta = 7d = 0.52\,\mathrm{mm}$. One curves gives us a measure of the Young modulus of the aggregate, however, this measure is often noisy due to the intrinsic variability of the aggregates. Therefore the effective Young modulus is averaged over a repetition of 15 measurements while rotating the aggregate between each measurement to probe undisturbed network at each time. This allows us to measure the mean effective Young modulus of the aggregate.

For Posidonia sea balls, the effective Young's modulus has been modeled [6, 14] to account for the fibrous properties of the aggregate. This model is derived by equating the bending energy of the fibres to the bending energy of a deformed sphere.

Similarly, the derivation of this model can be expressed in terms of forces: For a homogeneous body characterized by a Young's modulus E, the force associated with a displacement δ is given by $F_{\mathrm{h}} = \frac{4}{3} E R_{\mathrm{ind}}^{1/2} \delta^{3/2}$. This force must be identified to the force acting on the fibrous medium. The force on a single fibre can be expressed as $F_{\mathrm{f0}} = E_{\mathrm{f}} I L \kappa / w^2$, where E_{f} is the Young's modulus of a fibre, $I = \pi d^4/64$ is the moment of inertia of the fibre, and $w \sim (R_{\mathrm{ind}} \delta)^{1/2}$ [13] is the typical transverse distance over which bending occurs. Here, $\kappa = \delta / l$ represents the curvature of the fibre, with $l = L / \langle C \rangle = d/\phi$ [4] as the typical distance between contacts. The total force is then $F_{\mathrm{f}} = F_{\mathrm{f0}} N_{\mathrm{f}}$, where $N_{\mathrm{f}} = 4 w^3 \phi / (\pi d^2 L)$

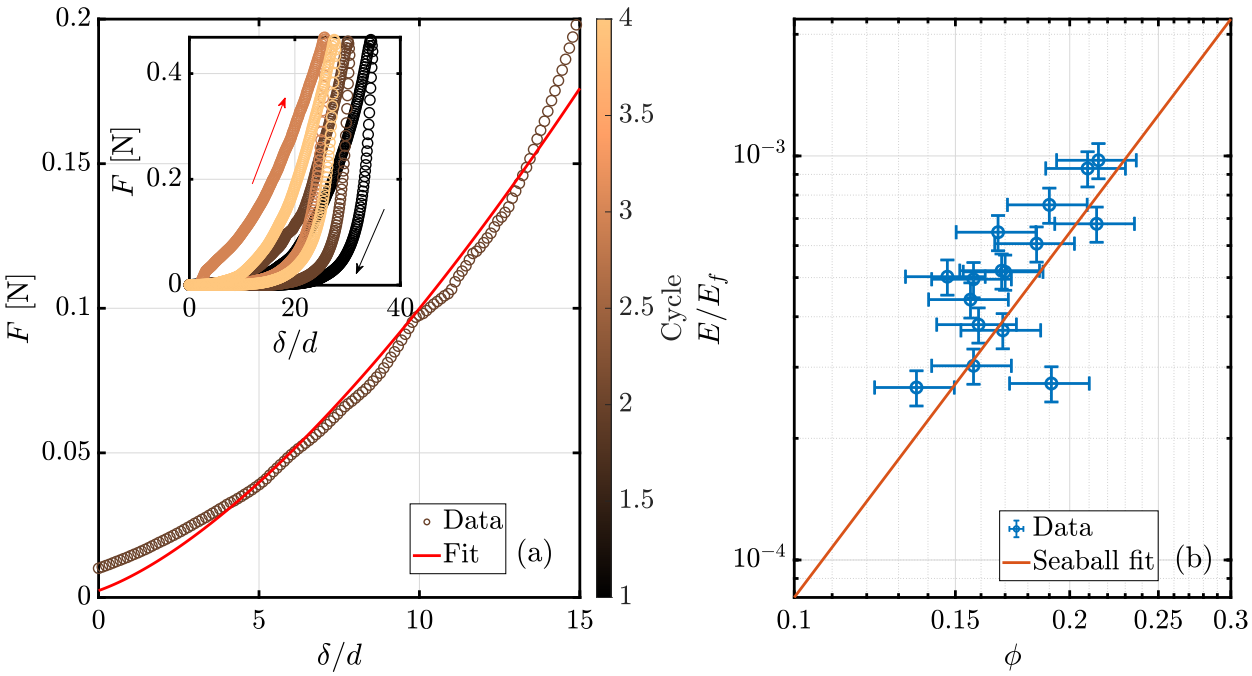


Figure 8: (a) Evolution of the force as a function of deformation, with a fit based on Hertz's law: $F = a(\delta - \delta_0)^{3/2}$. In the inset, four typical loading and unloading cycles are presented. The arrows indicate the direction of the hysteresis loop. (b) Evolution of the Young's modulus of the aggregate normalized by the Young's modulus of nylon fibres (tabulated as 2.9 GPa) as a function of the aggregate volume fraction. The error bars are estimated to represent 10% of the values for both ϕ and the Young's modulus. The red line corresponds to the fit obtained for Posidonia sea balls [6] : $E \sim \phi^3$, which agrees with our data quite well too.

represents the number of deflected fibres. Identifying these two forces yields

$$E \sim E_{\mathrm{f}}\phi^3 \tag{5}$$

This result is consistent with our experimental data, as shown in Figure 8 (b).

V. CONCLUSION

In this study, we have demonstrated the ability to create synthetic nylon fibre aggregates within a von Kármán turbulent flow. Using X-ray tomography, we characterized the density distribution of these aggregates. Our findings indicate that the density profile remains unchanged regardless of the formation parameters tested.

The mean volume fraction of the aggregates increases with their sizes as well as with the duration of the experiments. The observed volume fractions exceed those typically found in the random packing of rods [4].

The coordination number of the fibres follows a Γ distribution, with a mean contact number consistent with the scaling laws based on excluded volume argument [4]. Furthermore, the fibres within the aggregates are not randomly oriented; rather, the structure comprises two distinct regions: an inner core of randomly oriented fibres surrounded by an external shell of orthoradial fibres. Our curvature analysis suggests that entanglement driven by steric effects is a more plausible mechanism for the aggregation process than elastic interlocking in the case of our aggregates. Finally, mechanical indentation experiments, interpreted using an elastic sphere model, shows that the Young's modulus of the fibre aggregates depend on the volume fraction as $E \sim E_{\mathrm{f}}\phi^3$. This experimental results are fully consistent with previous findings for similar fibre aggregates [6].

---

[1] R. C. Picu, Mechanics of random fiber networks a review, Soft Matter **7**, 6768 (2011), publisher: The Royal Society of Chemistry.

[2] F. Karimi, P. Soltani, M. Zarrebini, and A. Hassanpour, Acoustic and thermal performance of polypropylene nonwoven fabrics for insulation in buildings, Journal of Building Engineering **50**, 104125 (2022).

[3] I. M. Hutten, *Handbook of Nonwoven Filter Media* (Elsevier, 2007) google-Books-ID: RzYgB-HumVdoC.

[4] A. P. Philipse, The Random Contact Equation and Its Implications for (Colloidal) Rods in Packings, Suspensions, and Anisotropic Powders, Langmuir **12**, 1127 (1996), publisher: American Chemical Society.

[5] A. Ekman, A. Miettinen, T. Tallinen, and J. Timonen, Contact Formation in Random Networks of Elongated Objects, Physical Review Letters **113**, 268001 (2014), publisher: American Physical Society.

[6] G. Verhille, S. Moulinet, N. Vandenberghe, M. Adda-Bedia, and P. Le Gal, Structure and mechanics of aegagropilae fiber network, Proceedings of the National Academy of Sciences **114**, 4607 (2017), publisher: Proceedings of the National Academy of Sciences.

[7] G. Bonnier and B. H. Library, *Revue générale de botanique*, Revue générale de botanique No. vol. 5 (Libraire générale de l'enseignement., 1893) pp. 65–73.

[8] N. Machicoane, L. Fiabane, R. Zimmermann, M. Bourgoin, J.-F. Pinton, and R. Volk, Dynamique lente de particules matérielles dans un écoulement de von Kármán, in *Rencontres du Non-Linéaire 2013* (Paris, France, 2013).

[9] S. R. Williams and A. P. Philipse, Random packings of spheres and spherocylinders simulated by mechanical contraction, Physical Review. E, Statistical, Nonlinear, and Soft Matter Physics **67**, 051301 (2003).

[10] J. Blouwolff and S. Fraden, The coordination number of granular cylinders, Europhysics Letters **76**, 1095 (2006), publisher: IOP Publishing.

[11] R. M. Soszynski and R. J. Kerekes, Elastic interlocking of nylon fibers suspended in liquid: Part 1. Nature of cohesion among fibers, Nordic Pulp & Paper Research Journal **3**, 172 (1988), publisher: De Gruyter.

[12] C. Brouzet, R. Guiné, M.-J. Dalbe, B. Favier, N. Vandenberghe, E. Villermaux, and G. Verhille, Laboratory model for plastic fragmentation in the turbulent ocean, Physical Review Fluids **6**, 024601 (2021), publisher: American Physical Society.

[13] Theory of Elasticity (Third Edition) (Butterworth-Heinemann, Oxford, 1986) p. iv.

[14] C. M. van Wyk, Note on the Compressibility of Wool, Journal of the Textile Institute Transactions **37**, T285 (1946).